

CO₂-assisted rapid synthesis of porphyrin-based Bi-MOFs for photocatalytic CO₂ reduction: An efficient strategy for carbon cycle

Mingjie Cheng^{a,1}, Bo Gao^{a,1}, Xiaoli Zheng^{a,*}, Wenzhuo Wu^b, Weiqian Kong^a, Pengfei Yan^b, Zubin Wang^a, Bin An^b, Yunpeng Zhang^a, Qingchao Li^a, Qun Xu^{a,b,**}

^a College of Materials Science and Engineering, Zhengzhou University, Zhengzhou 450052, PR China

^b Henan Institute of Advanced Technology, Zhengzhou University, Zhengzhou 450052, PR China



ARTICLE INFO

Keywords:

Metal-organic frameworks
Supercritical CO₂
Carbon cycle
CO₂ coordination
Photocatalytic CO₂ reduction

ABSTRACT

Exploring a facile, rapid and efficient route to produce metal-organic frameworks (MOFs) with highly accessible active sites is of great importance for catalysis. Here we demonstrate the CO₂ coordination can drive low temperature rapid synthesis of porphyrin-based bismuth-MOFs (Bi-PMOFs) by utilizing synergistic physical and chemical properties of supercritical CO₂ (SC-Bi-PMOFs). The molecular-level role of scCO₂ in the synthesis of SC-Bi-PMOFs have been investigated through a series of characterizations including *in-situ* time-dependent infrared spectroscopy, wherein chemical coordination of CO₂ promotes to fabricate 2D SC-Bi-PMOFs nanosheets. Moreover, the formation of Cu-PMOFs and Fe-PMOFs proves the universal scCO₂ strategy for synthesizing PMOFs. Density functional theory (DFT) calculations together with experiments results confirm the SC-Bi-PMOFs with abundant active sites guarantee efficient ligand-to-metal charge transfer and reduction efficiency of CO₂. The high-efficiency utilization of CO₂ for synthesizing a series of MOFs and subsequent catalysis on photocatalytic CO₂ reduction for valuable chemicals realize the carbon recycle.

1. Introduction

Sunlight-driven catalytic CO₂ reduction into valuable chemicals represents a desirable strategy to tackle energy crisis and environmental issues. Recently, metal-organic frameworks (MOFs) have aroused widespread interest in photocatalytic CO₂ reduction as their tunable pore structures, diverse fascinating topologies as well as excellent light-harvesting and reactant adsorption capabilities [1–3]. However, most MOF materials normally require harsh synthesized conditions (such as high temperature, high pressure or long reaction time) [4–7]. For example, the traditional solvothermal synthesis of ZIF-8 requires a reaction at 140 °C for 24 h [8], and vast solvents are required in the subsequent treatment to wash away the residual solvent and by-products in the pores [7,9]. Moreover, most bulk MOFs contain limited accessible active sites and sluggish mass transport in their inner pores [10]. These above reasons are obviously unfavorable for the application of MOFs-based photocatalysts in industrial scale. Therefore, exploring a facile manner to rapidly synthesize MOFs under mild conditions with

highly accessible active sites is exciting and imperative.

Two-dimensional (2D) MOFs are considered to be promising photocatalysts because of their high surface area, abundant exposed active sites, fast charge transfer and rapid mass transport properties [11,12]. Two major strategies for preparing of 2D MOFs include top-down exfoliation [13–16] and bottom-up methods [17–19]. Among these, bottom-up wet chemical method has been demonstrated to be an effective approach for synthesizing 2D MOF nanosheets in high yield [20,21]. However, the traditional bottom-up methods usually require the assistance of surfactant, which might be not easily removed and severely hinder the catalytic active sites [22,23]. Supercritical CO₂ (scCO₂) possess almost zero surface tension, high diffusion coefficient, low viscosity as well as easily available and recyclable properties [24]. Moreover, the product can be easily purified without the need for complex post-processing processes [25], and the utilization of scCO₂ can avoid pore collapse [26]. These fascinating physical properties make scCO₂ serving as a benign substitute for a number of solvents to synthesize MOF materials in a green and environmentally friendly way.

* Corresponding author.

** Corresponding author at: College of Materials Science and Engineering, Zhengzhou University, Zhengzhou 450052, PR China.

E-mail addresses: xzhengab@zzu.edu.cn (X. Zheng), qunxu@zzu.edu.cn (Q. Xu).

¹ M. Cheng and B. Gao contributed equally to this work.

[27–30]. Apart from the above outstanding physical properties of scCO₂, chemical-coordination effect of CO₂ molecules could facilitate chemical adsorption of CO₂ on the metal atoms [31]. Our previous works have demonstrated that scCO₂ possess the capability to realize top-down exfoliation of 3D MOFs into 2D MOFs through CO₂ chemical adsorption and ligand exchange strategy [14,15]. Nevertheless, few works have focused on investigating the synergistic physical and chemical effect of scCO₂ on the bottom-up synthesis of MOFs with highly accessible active sites [32]. Additionally, the detailed synthesized mechanism and the universal scCO₂ strategy for producing a certain class of MOFs have not been fully investigated. Moreover, most of these works mainly focus on studying traditional metal (e.g. Cu, Ni, Fe, Co)-based MOFs. Main group metal bismuth (Bi)-based catalysts hold great potential in CO₂ reduction in that Bi sites could efficiently inhibit the hydrogen evolution reaction and activate CO₂ [33,34]. Therefore, it is inspiring and meaningful to further study the scCO₂-synthesized Bi-MOFs with abundant active sites for photocatalytic CO₂ reduction and explore the possibility of carbon cycle.

As a proof of concept, the possibility of low temperature rapid synthesis of porphyrin-based Bi-MOFs (Bi-PMOFs) using TCPP (TCPP = 5,10,15, 20-tetras (carboxyphenyl) porphyrins) as ligands and Bi ions as metal clusters was explored for the first time under mild scCO₂ conditions (35 °C, 8 MPa, 2–6 h). Compared with traditional solvothermal synthesis in our previous study [34], 2D and 3D Bi-PMOFs can be quickly and simultaneously obtained under more mild conditions (temperature was reduced from 120 °C to 35 °C, reaction time was reduced from 12 h to 2 h) thanks to the synergistic physical and chemical effect of scCO₂. Furthermore, time-dependent infrared spectroscopy (IR) connected with a scCO₂ apparatus was utilized to in-situ dynamic investigate the molecular-level role of scCO₂ in the synthesis of Bi-PMOFs. In the subsequent photocatalytic reduction of CO₂, the catalytic efficiency was significantly improved by 1.5 times compared to the traditional solvothermal synthesized Bi-PMOFs. Moreover, the scCO₂ strategy was also applied to synthesize a series of M-PMOFs (M= Cu and Fe), verifying the universal application prospect of scCO₂ in the synthesis of porphyrin-based MOFs. This study provides new insights into the CO₂ coordination-driven low temperature rapid synthesis of porphyrin-based MOFs, and realizes the carbon cycle for efficiently photocatalytic CO₂ reduction.

2. Experimental section

2.1. Materials

5,10,15,20-tetrakis(4-carboxyphenyl) porphyrin (TCPP, 97 %, Shanghai Aladdin Biochemical Technology Co., Ltd.), bismuth nitrate pentahydrate (Bi(NO₃)₃•5 H₂O, 99 %, Xilong Scientific Co., Ltd.), Copper (ii) nitrate hydrate (Cu(NO₃)₂•3 H₂O Shandong Xiya Chemistry Industri Ltd.); Iron(III) nitrate nonahydrate (Fe(NO₃)₃•9 H₂O, Shanghai Aladdin Biochemical Technology Co., Ltd.), formic acid (HCOOH, 88 %, Tianjin Yongda Chemical Reagent Co., Ltd.), N,N-dimethylformamide (DMF, 99.5 %, Sinopharm Chemical Reagent Co., Ltd.), poly-vinylpyrrolidone (PVP, Beijing Wokai Biotechnology Co., Ltd.), trifluoroacetic acid (TFA, Shanghai Aladdin Biochemical Technology Co., Ltd.), acetonitrile (MeCN, 99 %, Shanghai Macklin Biochemical Technology Co., Ltd.), anhydrous ethanol (C₂H₅OH, 99.7 %, Sinopharm Chemical Reagent Co., Ltd.), triethanolamine (TEOA, 99 %, Sinopharm Chemical Reagent Co., Ltd.), sodium sulphate (Na₂SO₄, 99 %, Damao Chemical Reagent Factory). All reagents were purchased from commercial sources and used without further purification.

2.2. Material synthesis

2.2.1. Synthesis of SC-Bi-PMOF

For the synthesis of SC-Bi-PMOF using CO₂-assisted technology, 12.14 mg (0.025 mmol) of Bi(NO₃)₃•5 H₂O, 11 mg (0.014 mmol) of

TCPP, 50 μL of formic acid were dissolved in 40 mL of DMF–ethanol solution with a volume ratio of 3:1 under stirring. After that, the above solution was transferred into the autoclave at room temperature. Then CO₂ is charged into the autoclave under stirring to the desired pressure of 8 MPa for 2 and 6 h at 35 °C. The mixture solutions were collected via centrifugation at 8000 rpm for 10 min and further washed by ethanol three times. After drying overnight at 60 °C, the solid product was obtained. The resulting sample was named as SC-Bi-PMOF-2 h and SC-Bi-PMOF-6 h. SC-Bi-PMOF-6 h-PVP was prepared at the same condition (35 °C, 8 MPa, 6 h) in scCO₂ with the addition of 25 mg of PVP. Bi-PMOF-6 h prepared at the same condition (35 °C, 6 h) without scCO₂ was also provided for comparison.

2.2.2. Synthesis of T-Bi-PMOF-12 h

In a typical procedure, 12.14 mg (0.025 mmol) of Bi(NO₃)₃•5 H₂O, 11 mg (0.014 mmol) of TCPP, 50 μL of formic acid were dissolved in 40 mL of DMF–ethanol solution with a volume ratio of 3:1 under stirring. After that, the above solution was transferred into the autoclave at room temperature. Next, the sealed autoclave was heated at 120 °C for 12 h. The mixture solutions were collected via centrifugation at 8000 rpm for 10 min and further washed by ethanol three times. After drying overnight at 60 °C, the solid product was obtained. The resulting sample was named as T-Bi-PMOF-12 h.

2.2.3. Synthesis of SC-Cu-PMOF-6 h and T-Cu-PMOF-12 h

For the synthesis of SC-Cu-PMOF-6 h, 24 mg (0.1 mmol) of Cu (NO₃)₂•3 H₂O, 11 mg (0.014 mmol) of TCPP, 50 μL of formic acid were dissolved in 40 mL of DMF–ethanol solution with a volume ratio of 3:1 under stirring. After that, the above solution was transferred into the autoclave at room temperature. Then CO₂ is charged into the autoclave under stirring to the desired pressure of 8 MPa for 6 h at 35 °C. T-Cu-PMOF-12 h was obtained in the autoclave by heated for 12 h at 120 °C without scCO₂. The mixture solutions were collected via centrifugation at 8000 rpm for 10 min and further washed by ethanol three times. After drying overnight at 60 °C, the solid product was obtained.

2.2.4. Synthesis of SC-Fe-PMOF-6 h and T-Fe-PMOF-12 h

For the synthesis of SC-Fe-PMOF-6 h, 10 mg (0.025 mmol) of Fe (NO₃)₃•9 H₂O, 11 mg (0.014 mmol) of TCPP, 25 mg PVP, 100 μL of TFA were dissolved in 40 mL of DMF–ethanol solution with a volume ratio of 3:1 under stirring. After that, the above solution was transferred into the autoclave at room temperature. Then CO₂ is charged into the autoclave under stirring to the desired pressure of 8 MPa for 6 h at 35 °C. T-Fe-PMOF-12 h are obtained in the autoclave by heated for 12 h at 120 °C without scCO₂. The mixture solutions were collected via centrifugation at 8000 rpm for 10 min and further washed by ethanol three times. After drying overnight at 60 °C, the solid product was obtained.

2.3. Photocatalytic CO₂ reduction

The photocatalytic CO₂ reduction experiments were conducted in a 50 mL sealed glass reactor equipped with a quartz plate and gas inlets and outlets. In a typical photocatalytic experiment, 1.00 mg catalyst, 40 mL of MeCN and 1 mL of TEOA were mixed together under ultrasound and then transferred to the glass reactor. The solution was vigorous stirred and maintained at 25 °C by a cooling circulatory system. Afterwards, the glass reactor was purged with high purity CO₂ (20 mL/min) to remove the air and saturate the solution for 20 min. The light source for the photocatalytic reaction was a 300 W Xe lamp (cut 420 nm), and the light intensity was 500 mW cm⁻². During the photocatalytic process, the produced gas at different reaction time was continuously detected and quantified online by a gas chromatograph equipped with both TCD (Thermal conductivity detector) and FID (Flame ionization detector) detectors (flow rate of CO₂ at 7 mL/min).

2.4. Photoelectrochemical measurements

Photoelectrochemical measurements were performed in a H-cell equipped with an electrochemical station (CHI 660E). A standard three-electrode system was used for the electrochemical experiments, the FTO glass as photoelectrode, Pt foil as counter electrode, and Ag/AgCl electrode as reference electrode, respectively. The electrolyte was 0.5 M Na₂SO₄ aqueous solution and the geometrical surface area of working electrode was about 1 cm². The working electrode was prepared by the following steps: First, 2 mg of catalyst and 10 µL of Nafion (5 wt%) were added into 1.5 mL of alcohol solution. The mixture was sonicated for 30 min to disperse completely. 40 µL of the dispersion was then deposited onto FTO and dried under ambient conditions.

2.5. Computational methods

All the calculations are based on Density Functional Theory (DFT) as implemented in the Vienna Ab-initio Simulation Package (VASP) code [35,36] utilizing the projector augmented wave method (PAW) [37]. The exchange-correlation energy of generalized gradient approximation put forward by Perdew, Burke, and Ernzerhof (GGA-PBE) [38] is adopted. A vacuum of 15 Å perpendicularly to the sheets was applied to avoid the interaction between layers. A kinetic energy cutoff of 400 eV is used for the plane-wave basis set. The sampling in the Brillouin zone was set with 1×1×2 by the Monkhorst-Pack method [39]. Convergence criteria employed for both the electronic self-consistent relaxation and ionic relaxation are set to be 10⁻⁴ and 0.05 eV/Å for energy and force, respectively.

The Gibbs free energy change (ΔG) for each step was calculated as follows:

$$\Delta G = \Delta E + \Delta ZPE - T\Delta S \quad (T = 298.15 \text{ K})$$

where ΔE , ΔZPE , and ΔS are the changes in the reaction energy, zero-point energy, and entropy, respectively.

The zero-point energy and entropy correction were obtained from the NIST-JANAF thermodynamics table for gas molecules, and by calculating the vibrational frequencies for the intermediate adsorbates, respectively.

2.6. Characterization

Scanning electron microscopy (SEM) images were obtained using a Zeiss Sigma 300. Transmission electron microscopy (TEM) images were recorded using a FEI Talos F200X G2 microscope. X-ray diffraction (XRD) patterns were carried out with Rigaku SmartLab SE. X-ray photoelectron spectroscopy (XPS) spectra were collected on a Thermo Scientific K-Alpha Spectrometer. Photoelectrochemical (PEC) performance were evaluated on CHI 660E electrochemical workstation. UV/Vis diffuse reflectance spectra was measured by using a UV-3600 Plus UV/Vis-NIR spectrometer (Shimadzu). Raman measurements were performed using LabRAM HR Evolution with laser wavelength of 532 nm. The Fourier-transform infrared (FT-IR) spectra were obtained on an FT-IR spectrometer (Prestige 21; Shimadzu) in a KBr pellet at room temperature. Invenio-R FT-IR spectrometer (Bruker, USA) connected to a scCO₂ reactor was used to in-situ record the IR spectra of the CO₂-assisted synthetic process. The in-situ FT-IR test of photocatalytic reduction of CO₂ was conducted using a Bruker INVENIOS FT-IR spectrometer equipped with a Xe lamp light source and in-situ cell (10 mg of the sample was placed in the in-situ cell, CO₂ and H₂O mixed gas was passed through for 30 min to reach adsorption equilibrium before test). The PL spectra was recorded at room temperature on a (Shimadzu) RF-6000 spectrophotometer. The NMR spectra were performed by a ¹H NMR spectrometer (AVANCE III 400 MHz).

3. Results and discussion

3.1. Bottom-up production of 2D and 3D Bi-PMOFs through synergistic effect of scCO₂

At present, the traditional solvothermal synthesis strategy can only produce 3D bulk Bi-PMOFs structure and require high temperature (120 °C) and long reaction time (12 h) [34]. Herein, take full advantage of chemical and physical synergistic effect of scCO₂, 2D Bi-PMOF nanosheets and 3D Bi-PMOF bulks can be obtained simultaneously under mild conditions (35°C, 2–6 h, 8 MPa). The schematic illustration of scCO₂-assisted rapid synthesis of 2D and 3D Bi-PMOFs is shown in Fig. 1. In the case of Bi-PMOFs, each Bi³⁺ is octahedrally coordinated with four carboxyl groups from different TCPP linkers and two oxygen atoms from OH group[34]. From a physical standpoint, thanks to the high-diffusion and anti-solvent property, scCO₂ might greatly influence the reaction kinetics and accelerate the polymerization of Bi-PMOFs through increasing the diffusion and transport of the precursors/by-products as well as promoting nucleation and crystal growth [29,30]. Thus, Bi-PMOFs can be obtained rapidly at low reaction temperature. From a chemical point of view, CO₂ can act as a Lewis base and donate electrons to Lewis acidic metal ions through O-M coordination, then the CO₂ molecules could accept a bent configuration and coordinate to one or two metal centers through one or two O atoms (monodentate or bidentate mode) [15,40]. In principle, the synthesis of 2D MOF nanosheets can be realized by restricting the growth of the MOF crystals in one direction, or by limiting/suppressing the crystalline interlayer interactions during synthesis [20]. During the scCO₂ synthesis process of Bi-PMOFs, the CO₂ chemical coordination layer can efficiently induce steric hindrance effect and block the spatial-growth of the 3D Bi-PMOFs, thus facilitate the synthesis of 2D Bi-PMOF nanosheets. The resulting rapid synthesis of 2D and 3D Bi-PMOFs with well-exposed active sites and fast charge/mass transfer capability is prone to display highly enhanced photocatalytic CO₂ reduction activity, realizing the carbon cycle.

3.2. Structural characterization of SC-Bi-PMOFs

To validate the synergistic effect of scCO₂ on the synthesis of Bi-PMOFs, structural characterization including powder X-ray diffraction (XRD), scanning electron microscopy (SEM) and transmission electron microscopy (TEM) were conducted. Herein, for convenience, we designate various scCO₂-synthesized Bi-PMOFs as “SC-Bi-PMOF-xh”, where x refers to the reaction time. Bi-PMOF-6 h prepared at the same condition (35 °C, 6 h) without scCO₂ and T-Bi-PMOF-12 h prepared with

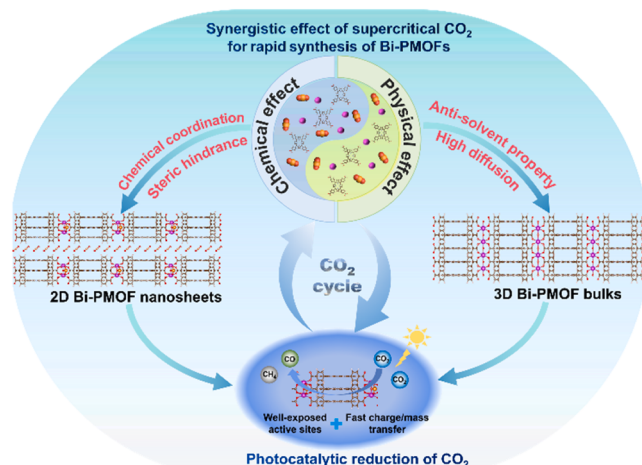


Fig. 1. Schematic illustration of scCO₂-assisted bottom-up rapid synthesis of 2D and 3D Bi-PMOFs and photocatalytic reduction of CO₂ for realizing CO₂ cycle.

traditional solvothermal method (120°C , 12 h) were also provided for comparison. As depicted in Fig. 2a, the XRD patterns of the SC-Bi-PMOF samples match well with the simulated diffraction pattern of Bi-PMOF [34]. By prolonging the scCO_2 reaction time, the SC-Bi-PMOF-6 h only exhibit slight crystallinity enhancement compared to the SC-Bi-PMOF-2 h based on the slightly reduced full width at half maximum of (110) crystal plane. However, Bi-PMOFs-6 h prepared without scCO_2 exhibits quite poor XRD pattern and the main peaks almost disappear, showing that the scCO_2 is indispensable for the rapid synthesis of Bi-PMOFs.

The microscopic structure of the as-prepared SC-Bi-PMOFs was investigated by SEM, TEM and HRTEM. As shown in Figs. 2b, 3D bulk structure with lateral dimensions ranging from 300 to 400 nm and 2D nanosheets co-exist in the SC-Bi-PMOF-2 h, and the ratio of the 2D Bi-PMOFs is about 56.3 %. The TEM images in Fig. 2c-f also manifest that two kinds of structures exist. The high resolution TEM (HRTEM) image in Fig. 2d (the area taken from the edge of the 3D bulk in Fig. 2c) shows that the lattice spacings are 0.56 nm, assigned to the (300) plane of Bi-PMOFs. Furthermore, a typical 2D layer structure of Bi-PMOFs with (002) interlayer spacing of 0.82 nm can be observed in Fig. 2f (the area designated by the red square box in Fig. 2e), and the Bi-PMOFs nanosheets mainly consist of less than 10 layers. In addition, the SC-Bi-PMOF-6 h has similar sample size and ratio of 2D Bi-PMOFs with those of SC-Bi-PMOF-2 h (Figure S1a). It means that the synthesis of 2D Bi-PMOF nanosheets is independent of reaction time. However, Bi-PMOF-6 h prepared without scCO_2 shows nano-bulks and no 2D Bi-PMOFs is observed (Figure S1b), suggesting that scCO_2 play indispensable role in the synthesis of Bi-PMOFs, especially for the 2D Bi-PMOFs. Moreover, when the reaction is conducted under traditional solvothermal method (T-Bi-PMOF-12 h), only 3D bulk Bi-PMOFs are obtained (Figure S1c), further implying that scCO_2 play key roles in the formation of 2D Bi-PMOF nanosheets. To increase the ratio of 2D Bi-PMOF nanosheets,

we also added PVP during the synthesis of Bi-PMOFs in the scCO_2 (SC-Bi-PMOF-6 h-PVP), and the ratio of the 2D Bi-PMOF nanosheets can be increased to above 75 % (Figure S1d). Elemental mappings images reveal the uniform distribution of Bi, C, N and O elements across the entire 3D bulk (Figs. S2) and 2D Bi-PMOFs (Figure S3). And the corresponding elemental compositions show that the atomic ratios of Bi in 3D bulk and 2D Bi-PMOFs are 2.6 % and 5.5 %, respectively, clearly showing that 2D nanosheets provides the possibility of more exposed Bi active sites.

Attenuated total reflection infrared (ATR-IR) spectroscopy is an important technology to monitor the molecular vibrational information and analyze the band changes induced by adsorbates. Herein, ATR-IR spectroscopy connected to the scCO_2 reactor was utilized to in-situ investigate the effect of scCO_2 on the synthesis of the Bi-PMOFs. Fig. 3a presents the time-dependent ATR-IR spectra collected from the reaction system. Before CO_2 injection (25°C and 35°C), four vibrational modes associated with $\text{C}=\text{O}$ asymmetric and symmetric stretching $\nu_{\text{as}}(\text{C}=\text{O})$ and $\nu_{\text{s}}(\text{C}=\text{O})$, $\text{C}-\text{OH}$ stretching $\nu(\text{C}-\text{OH})$, and $\text{C}=\text{O}$ bending $\delta(\text{C}=\text{O})$ vibrations of the carboxyl group (-COOH) in the TCPP ligands are observed at 1662 , 1384 , 1257 and 795 cm^{-1} , respectively [41,42]. Additionally, the peaks at 1494 and 1088 cm^{-1} are corresponding to $\text{C}-\text{N}$ stretching and $\text{C}-\text{H}$ asymmetric bending vibrations, respectively [43]. The $\text{C}-\text{H}$ bending modes $\delta(\text{CH})$ of the phenyl rings are also observed at 767 and 655 cm^{-1} [44]. Once the CO_2 is injected into the reactor and the pressure reaches 8 MPa , the -COOH vibration modes of the TCPP ligands exhibit obvious blueshift (from 1662 , 1384 , 1257 and 795 cm^{-1} to 1682 , 1388 , 1266 and 811 cm^{-1}), suggesting the change of chemical environment around -COOH groups [45,46]. At the same time, a strong new stretching vibration peak of Bi-O bond appears at 586 cm^{-1} [47,48]. It has been reported that strong metal-carboxylate (M-O) interactions should cause blueshifts to carboxylate stretches [49]. The blueshift of the carboxylate groups and the presence of Bi-O after CO_2

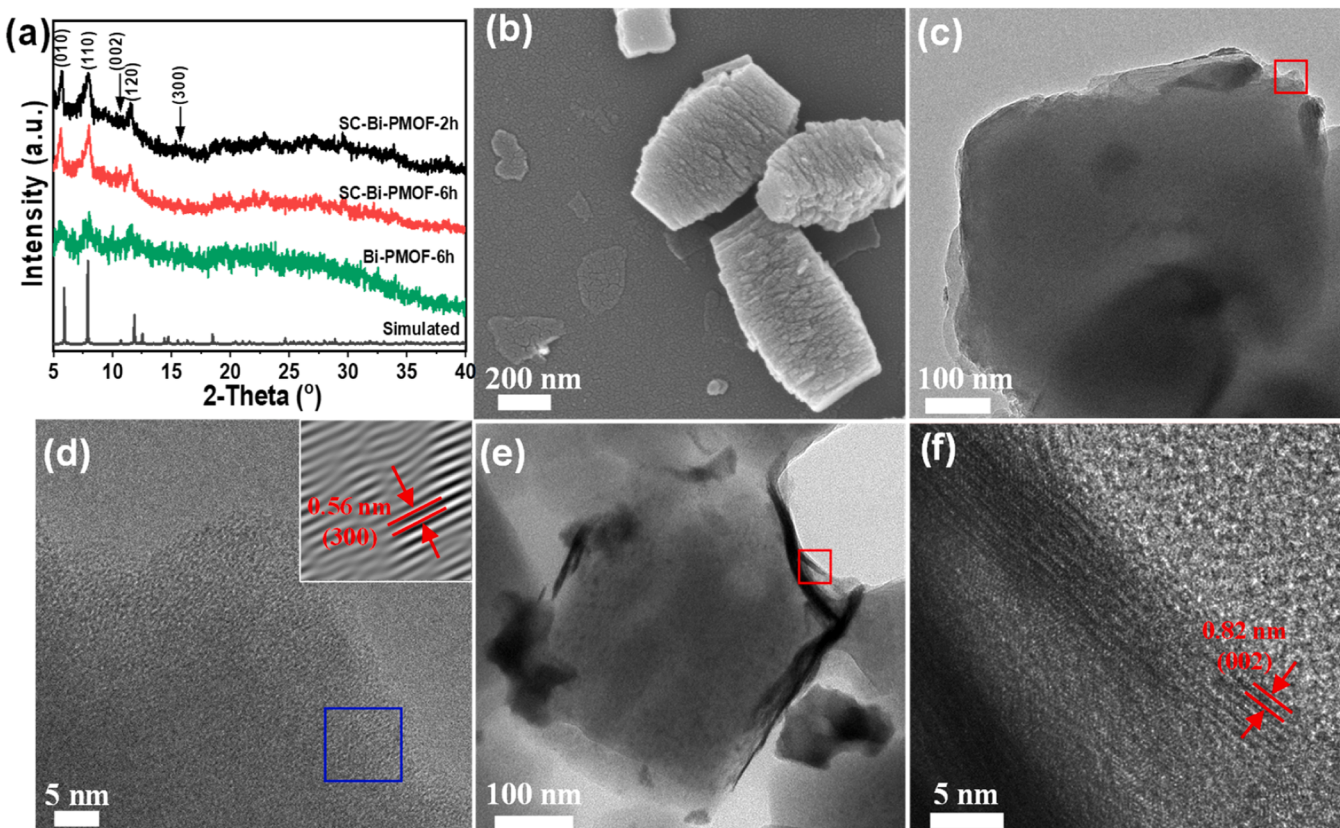


Fig. 2. (a) XRD patterns of SC-Bi-PMOF-2 h, SC-Bi-PMOF-6 h, Bi-PMOF-6 h and the simulation pattern of Bi-PMOF. (b) SEM image of SC-Bi-PMOF-2 h. (c, e) TEM images of SC-Bi-PMOF-2 h. (d, f) HRTEM images of red square box enclosed in (c, e). Inset in (d) is FFT image of blue square box enclosed in (d).

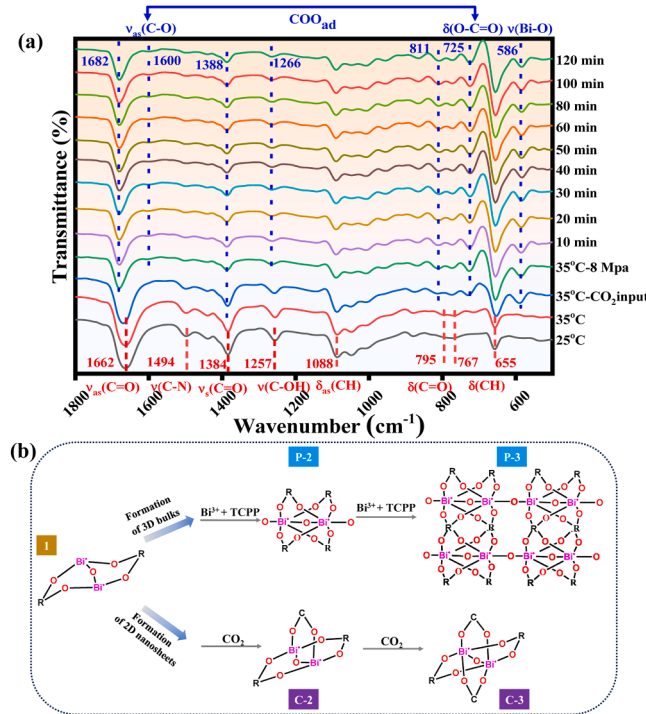


Fig. 3. (a) Time-dependent ATR-IR spectra of synthesized reaction system of Bi-PMOFs. The pristine reaction system contains precursors and formic acid in DMF/ethanol solution ($v/v = 3:1$). The pristine vibrational bands of the reaction system (red) and the new emerging bands induced by scCO₂ (blue). (b) The proposed mechanism of synergistic effect of CO₂ on the formation of 2D and 3D Bi-PMOFs (R represents the TCPP ligands).

injection clearly demonstrates that Bi ions/clusters are rapidly coordinated with the -COOH of TCPP ligands with the assistance of scCO₂, which could be benefit for the rapid synthesis of Bi-PMOFs efficiently in a short time. To prove this point, we also prepare Bi-PMOFs in scCO₂ for 0.5 h (SC-Bi-PMOF-0.5 h, Figure S4). As shown in Figs. S4a, 2D nanosheets and 3D bulks with smaller size than that of SC-Bi-PMOF-2 h are obtained in the SC-Bi-PMOF-0.5 h. The XRD pattern in Figure S4b also matches well with the SC-Bi-PMOF-2 h. Moreover, the yields of the SC-Bi-PMOFs decrease significantly with shortening reaction time and the yield is plateaued after 2 h (30.0 %, 35.5 % and 36.9 % for SC-Bi-PMOF-0.5 h, SC-Bi-PMOF-2 h and SC-Bi-PMOF-6 h, respectively). The above results demonstrate that SC-Bi-PMOFs can be rapidly synthesized in a short time with the assistance of scCO₂, and the crystal sizes and yields increase with the reaction time.

Notably, two new bands at 1600 and 725 cm⁻¹ are corresponding to the asymmetric stretching and bending vibration of chemical-adsorbed CO₂ (COO_{ad}), showing that chemical coordination between CO₂ and Bi-PMOF is present in the scCO₂ reaction system [41]. Our group has proved that CO₂ molecule is prone to coordinate with two adjacent metal ions as a bridging bidentate ligand (COO_{ad}) through ab initio molecular dynamics simulation, which is conducive to the formation of 2D MOFs [15]. To further validate the role of scCO₂ in the formation of Bi-PMOFs, time-dependent ATR-IR spectra of reaction system without scCO₂-treatment was also conducted. As shown in Figure S5, the characteristic -COOH vibrational frequency of the TCPP ligands are almost unchanged and there are no new peaks correlated with the chemical-coordinated CO₂ and Bi-O bands appear. These results strongly confirm that the necessary effect of scCO₂ for synthesizing Bi-PMOFs efficiently and obtaining 2D Bi-PMOF nanosheets without surfactant addition. Fig. 3b depicts the molecular structural evolution of scCO₂-assisted bottom-up synthesis of 2D and 3D Bi-PMOFs. First, the Bi³⁺ ions react with the deprotonated TCPP to construct the nanosized

framework building blocks (structure 1). Thanks to the unique physical properties of scCO₂, fast mass transfer and nucleation facilitate the formation of 3D Bi-PMOF bulks rapidly at mild reaction condition (from structure P-1 and P-2). On the other hand, CO₂ molecules acting as Lewis base chemically adsorb on the Bi metal centers through O-M coordination, and form chemical-adsorbed intermediate *COO (structure C-2). Finally, more and more CO₂ molecules adsorb on the Bi metal centers, the chemical coordination effect of CO₂ induces steric hindrance effect and blocks the spatial-growth of the 3D Bi-PMOFs, thus facilitates the synthesis of 2D Bi-PMOF nanosheets (Structure C-3) [50]. The above mechanistic analysis clearly demonstrates a fascinating strategy to rapid synthesis of 2D and 3D Bi-PMOFs with well-exposed active sites though the synergistic physical and chemical effect of scCO₂.

The detail chemical and electronic structure information of SC-Bi-PMOFs were further investigated by X-ray photoelectron spectroscopy (XPS), Raman spectra and UV-vis absorption spectroscopy. As shown in Fig. 4a, the high resolution Bi 4 f spectrum of T-Bi-PMOF-12 h shows the characteristic double peaks of Bi³⁺ at 165.0 and 159.7 eV. The Bi³⁺ peaks of the SC-Bi-PMOFs shift toward to lower binding energy, demonstrating electron transfer from the chemical coordinated CO₂ to the Bi cluster. The contents of Bi atoms estimated from the XPS are 3.9 %, 3.6 % and 2.8 % for SC-Bi-PMOF-2 h, SC-Bi-PMOF-6 h and T-Bi-PMOF-12 h, respectively. It further confirms that the chemical coordinated CO₂ facilitates the construction of 2D SC-Bi-PMOF nanosheet and provides more accessible Bi active sites. Similarly, in the O 1 s XPS spectra (Fig. 4b), the main C=O and Bi-O peaks of the SC-Bi-PMOFs also shift towards lower binding energies compared to that of T-Bi-PMOF-12 h. Furthermore, the contents of Bi-O in the SC-Bi-PMOF-2 h (15.8 %) and SC-Bi-PMOF-6 h (17.6 %) are quite higher than that of T-Bi-PMOF-12 h (3.4 %), indicating that more Bi sites are coordinated with the CO₂ and carboxyl groups of TCPP in the SC-Bi-PMOFs thanks to the synergistic effect of scCO₂. The abundant accessible Bi active sites enrich the electron distribution in the SC-Bi-PMOFs, which might be favor the subsequent electron transfer for CO₂ reduction. The N 1 s and C 1 s spectra of the samples are also provided in Figure S6, the SC-Bi-PMOFs exhibit the similar characteristic peaks as the T-Bi-PMOF-12 h. Notably, the absence of Bi-N and no obvious peak shift in the N 1 s XPS spectra prove that the porphyrin rings is not metallized by Bi ions [17].

Raman spectra were employed to better understand the chemical structure of the samples. As shown in Fig. 4c, the SC-Bi-PMOF samples exhibit similar Raman spectra as that of T-Bi-PMOF-12 h. The characteristic peaks for the TCPP ligands (i.e. phenyl, C-H, C-OH, N-H, pyrrole groups) are well present in the samples [51]. Moreover, the presence of Bi-O band at around 220 cm⁻¹, as well as the almost disappeared TCPP aggregates at around 325 cm⁻¹ and in-plane bending of C-OH at 1182 cm⁻¹, verify that Bi-PMOFs can also be prepared at low temperature and short time with the assistance of scCO₂ [34,52]. Notably, the peaks of N-H and pyrrole groups of the SC-Bi-PMOFs red-shift compared with that of T-Bi-PMOF-12 h (Figure S7), indicating that charge density redistribution occurs in SC-Bi-PMOFs due to the construction of 2D Bi-PMOFs [53]. The UV-vis absorption spectroscopy was further carried out to evaluate the electronic states of the SC-Bi-PMOFs. As shown in Fig. 4d, the soiret band at 370–500 nm and four Q-bands at 500–700 nm of the porphyrin unit are well preserved in the Bi-PMOFs, which may result in efficient light capture ability. In addition, the four Q-bands of the SC-Bi-PMOFs exhibit a blue shift compared with the T-Bi-PMOF-12 h. The blueshift can be ascribed to the formation of 2D Bi-PMOF nanosheets, which can shorten the electron transport distance and change the in-plane d-π conjugations and the out-of-plane π-π interactions in the SC-Bi-PMOFs [54,55].

The above results verify that the scCO₂-assisted strategy has been successfully performed to synthesize 2D and 3D Bi-PMOFs rapidly at low temperature. More importantly, this strategy can also synthesize 2D Cu-PMOFs and Fe-PMOFs. The XRD of the SC-Cu-PMOF-6 h and SC-Fe-PMOF-6 h are almost identical with that of T-Cu-PMOF-12 h and T-Fe-PMOF-12 h as well as other reported works (Figure S8a,b) [19,42]. The

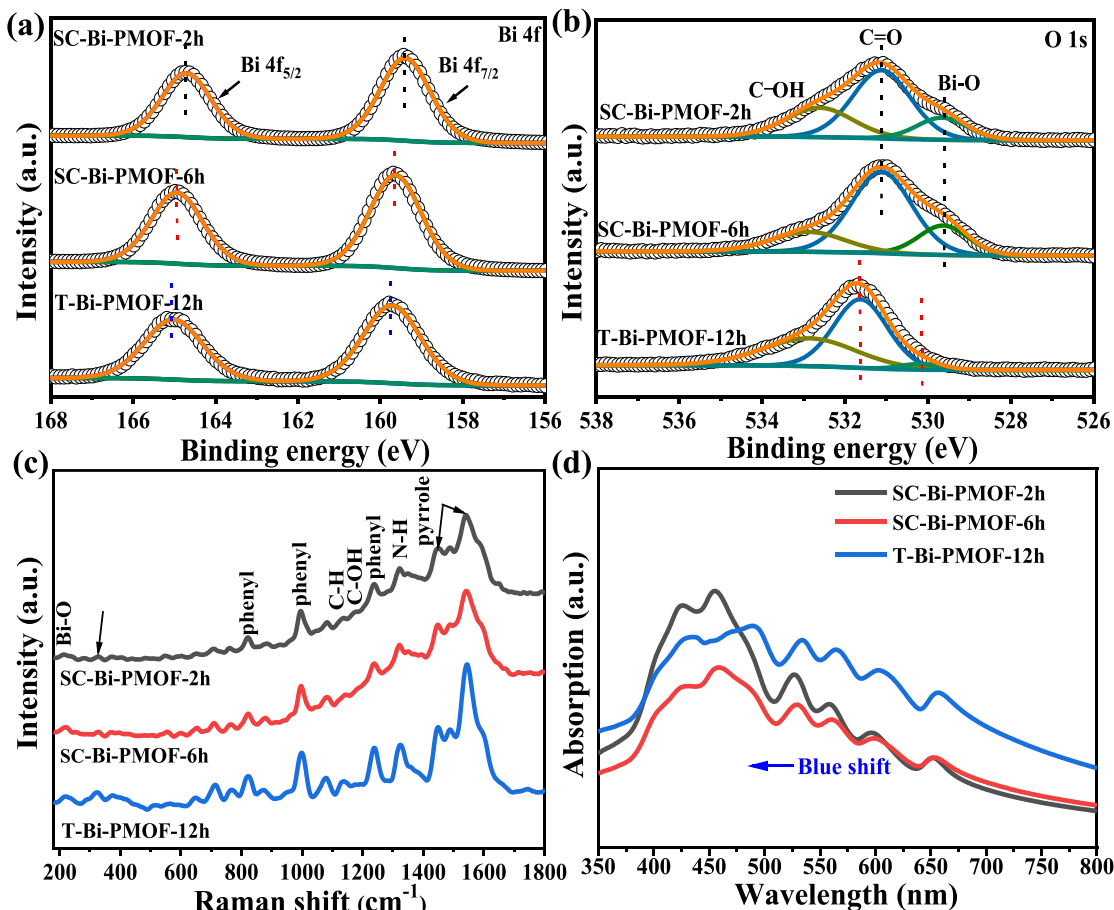


Fig. 4. High resolution XPS spectra of (a) Bi 4 f, (b) O 1 s of SC-Bi-PMOF-2 h, SC-Bi-PMOF-6 h and T-Bi-PMOF-12 h. (c) Raman spectra, (d) UV-vis absorption spectra of SC-Bi-PMOF-2 h, SC-Bi-PMOF-6 h and T-Bi-PMOF-12 h.

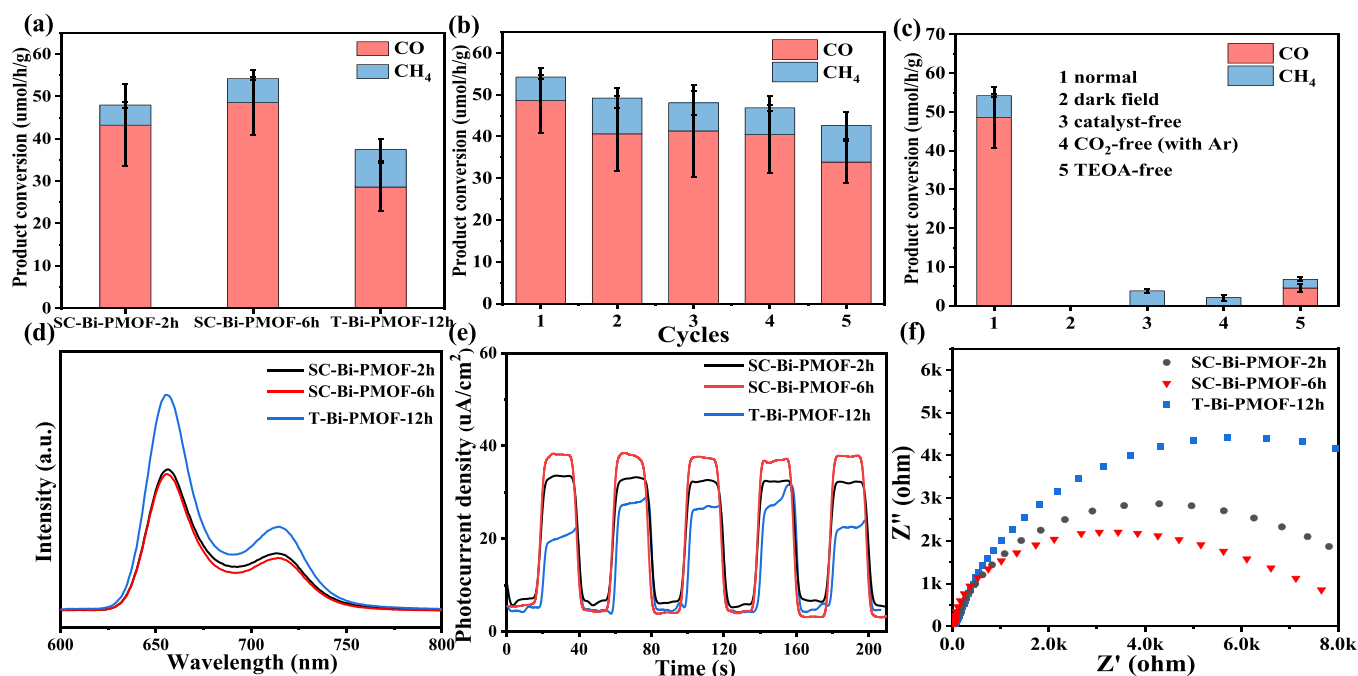


Fig. 5. (a) Photocatalytic performances of SC-Bi-PMOF-2 h, SC-Bi-PMOF-6 h, and T-Bi-PMOF-12 h. (b) Five cycles of CO₂ reduction over the SC-Bi-PMOF-6 h. (c) Photocatalytic performances of SC-Bi-PMOF-6 h at different conditions. (d) Steady-state PL spectra, (e) photocurrent-time (I-t) curves and (f) EIS Nyquist plots of SC-Bi-PMOF-2 h, SC-Bi-PMOF-6 h and T-Bi-PMOF-12 h.

SEM images show that 2D SC-Cu-PMOF-6 h nanosheets and SC-Fe-PMOF-6 h nanostrips can also be prepared under mild scCO₂ conditions (Figure S8c,d), revealing that the CO₂ chemical coordination-driven 2D structure is also applicable to other metallic porphyrin MOFs. Meanwhile, the 2D SC-Cu-PMOF-6 h and SC-Fe-PMOF-6 h also exhibit similar FTIR and Raman spectra with that of T-Cu-PMOF-12 h and T-Fe-PMOF-12 h (Figure S9), confirming the universality of scCO₂-assisted strategy in synthesizing porphyrin-based MOFs.

3.3. Photocatalytic CO₂ reduction performance of SC-Bi-PMOFs

The photocatalytic reduction of CO₂ over different photocatalysts was conducted under visible-light irradiation ($\lambda \geq 420$ nm), where TEOA was used as a sacrificial agent. As shown in Fig. 5a, compared with the T-Bi-PMOF-12 h, the photocatalytic performances of SC-Bi-PMOFs have been significantly improved. The decreased photocatalytic performance of SC-Bi-PMOF-0.5 h (Figure S10) might be resulted from the incomplete crystal structure coordination due to too short reaction time, which lead to unfavorable ligand-to-metal charge transfer [56]. And the residual PVP molecules adsorbed on the surface of Bi-PMOFs might severely hinder the catalytic active sites of SC-Bi-PMOF-6 h-PVP, thus also lead to inferior photocatalytic performance [57]. It is worth noting that the total CO and CH₄ yields of SC-Bi-PMOF-2 h (48.0 $\mu\text{mol}\cdot\text{h}^{-1}\text{g}^{-1}$) and SC-Bi-PMOF-6 h (54.3 $\mu\text{mol}\cdot\text{h}^{-1}\text{g}^{-1}$) is 1.3 and 1.5 times than that of T-Bi-PMOF-12 h (37.4 $\mu\text{mol}\cdot\text{h}^{-1}\text{g}^{-1}$). In view of SC-Bi-PMOF-6 h has similar morphology and chemical structure as that of SC-Bi-PMOF-2 h, the enhanced photocatalytic CO₂ reduction performance of SC-Bi-PMOFs-6 h than that of SC-Bi-PMOFs-2 h might be resulted from its slightly increased crystallinity, which can further promote the charge transport [58]. ¹H NMR spectroscopy (Figure S11) is applied to analyze the possible carbon-containing liquid product and no liquid product is detected, indicating that CO and CH₄ are the main reduction products and the average yields of the products are listed in Table S1. Table S2 summarizes the photocatalytic CO₂ reduction performance comparisons between SC-Bi-PMOFs and other reported catalysts, the yield of CO₂ reduction products in this work outperform most of the reported MOFs-based photocatalysts. As shown in Fig. 5b, the SC-Bi-PMOF-6 h exhibits good stability during the catalytic cycles, and there is only a slight decrease after five successive runs. The XRD, FTIR and Raman spectra analysis show that the structure of catalysts remains well after the photocatalytic reduction reaction (Figure S12). Additionally, a series of contrast experiments are conducted and shown in Fig. 5c. The results clearly demonstrate that the catalyst, light source, CO₂ and sacrificial agent TEOA are indispensable for the photocatalytic reduction of CO₂ to CO and CH₄.

3.4. Photocatalytic mechanism analyses

To elucidate the mechanism of excellent photocatalytic activity of SC-Bi-PMOFs, the energy band structures were estimated to evaluate the semiconductor properties of the catalysts. The energy gaps (E_g) estimated from the diffuse reflectance spectra by Tauc plots are 2.89 eV, 2.80 eV and 2.87 eV for SC-Bi-PMOF-2 h, SC-Bi-PMOF-6 h and T-Bi-PMOF-12 h, respectively (Figure S13). Besides, the valence band edge (E_{VB} , NHE) is calculated by the equation: $E_{VB, NHE} = \varphi + E_{VB, XPS} - 4.44$, where $E_{VB, XPS}$ is measured by the XPS-VB experiment (insets of Figure S13) and φ is the work function of the instrument (4.2 eV) [59]. Then the conduction band edge (E_{CB}) is calculated by $E_{CB} = E_{VB, NHE} - E_g$. Accordingly, the energy band structure diagrams are listed in Figure S14. Clearly, the three catalysts possess the similar band gap structures and the E_{CB} is higher than the reduction potentials of CO and CH₄, demonstrating that all the Bi-PMOFs possess favorable ability to photocatalytic reduction of CO₂ under visible light.

Furthermore, the steady-state photoluminescence (PL) emission spectra were measured to study the photogenerated electron-hole

recombination information of the catalysts (Fig. 5d). Obviously, the SC-Bi-PMOFs exhibit lower PL intensity than that of T-Bi-PMOF-12 h and SC-Bi-PMOF-6 h has the lowest one, which are consistent with the photocatalytic CO₂ reduction performance. It indicates that the present of 2D SC-Bi-PMOF nanosheets in the SC-Bi-PMOFs mainly contribute to the strikingly attenuated PL intensity, wherein the more accessible Bi active sites facilitate the effective charge transfer and reduced electron-hole recombination. The lowest PL intensity of SC-Bi-PMOF-6 h might be resulted from its slightly increased crystallinity, which can further promote the charge transport. To further unveil their e-h separation and transport efficiency, photocurrent density measured in cyclic dark and light intervals and electrochemical impedance spectroscopy (EIS) have been also performed (Fig. 5e,f). As expected, the SC-Bi-PMOFs exhibit higher photocurrent density and smaller semicircular radius of EIS Nyquist curves than that of T-Bi-PMOF-12 h, indicating that the enhanced charge separation and transfer efficiency play a dominate role in much higher photocatalytic CO₂ reduction performance of SC-Bi-PMOFs. Therefore, the above results clearly demonstrates that the rapid synthesis of 2D and 3D Bi-PMOFs with well-exposed active sites though the synergistic physical and chemical effect of scCO₂ contribute to the superior activity of photocatalytic CO₂ reduction.

To investigate the photocatalytic reaction mechanism, in-situ FT-IR test of photocatalytic CO₂ reduction was conducted to monitor the reaction intermediates on the SC-Bi-PMOF-6 h catalyst (Fig. 6a). As shown in Fig. 6a, there is almost no peak before light irradiation. The obvious peak located at 1664 cm⁻¹ appears after reaching the adsorption equilibrium, which is defined as H₂O [60]. The peaks at 1330 and 1391 cm⁻¹ are assigned to the bidentate carbonate (b-CO₃²⁻) and monodentate carbonates (m-CO₃²⁻), respectively [61]. The peaks corresponding to *CO₂ are at 1253 and 1707 cm⁻¹ [62,63], *COOH is at 1587 and 1620 cm⁻¹ [64], HCO₃ is at 1112, 1200 and 1412 cm⁻¹ [60], which are considered as key intermediates in the formation and conversion of *CO into CO [65,66]. In addition, the peaks at 1033, 1482 and 1158 cm⁻¹ are attributed to *CHO, *CH₂O and *OCH₃, which are the key intermediates of CO₂ photoreduction to CH₄ [63,67]. These peaks strength remain stable under light irradiation, indicating efficient adsorption of CO₂ molecules and intermediates on the catalyst surface, which is favorable to photocatalytic CO₂ reduction to CO and CH₄ [62].

Density functional theory (DFT) calculations were also performed to further understand the reaction mechanism of CO₂ reduction on the Bi-PMOFs. The CO₂ adsorption energy on the catalyst surface is first analyzed (Figure S15). The Bi-site readily interact with the O atoms of CO₂ through Bi-O bond, and the calculated CO₂ adsorption energy is -0.21 eV and the bond angle of the O=C=O bond is distinctly bent from 180° to 126.3°, revealing that CO₂ adsorption process on the surface of Bi-PMOFs is exothermic and the Bi active sites can capture and activate the CO₂ efficiently.

The Gibbs free energy of CO₂ to key intermediates of CO and CH₄ as well as the reaction pathway and the optimized structures on active sites were also calculated. As shown in Fig. 6b, the absorbed CO₂ on the Bi sites of Bi-PMOFs is activated and hydrogenated to produce *COOH spontaneously with a free energy of -0.15 eV. The positive free energy for the conversion of *COOH to *CO and CO desorption, indicating this step is the rate-limiting step. Moreover, the energy required for the conversion of *CO to *COH is 0.85 eV, which is lower than that required for the conversion of *CO to CO (1.31 eV), suggesting that the catalytic reaction pathway can also be further proceeded to produce CH₄.

On the basis of the above investigations, we propose the mechanism of overall photocatalytic CO₂ reduction on the SC-Bi-PMOFs (Fig. 6c). The porphyrin ligands serve as the light harvester and generate electron-hole pairs [68]. Photogenerated electrons rapidly transfer to the Bi active sites. The abundant electrons harvested at Bi active sites reduce CO₂ to CO and CH₄ (a ligand-to-metal charge transfer process) [42]. During the entire process, the presence of 2D nanosheets with highly accessible active sites ensure efficient electron transfer, which playing a key role in the multi-electron-involved photocatalytic CO₂ reduction.

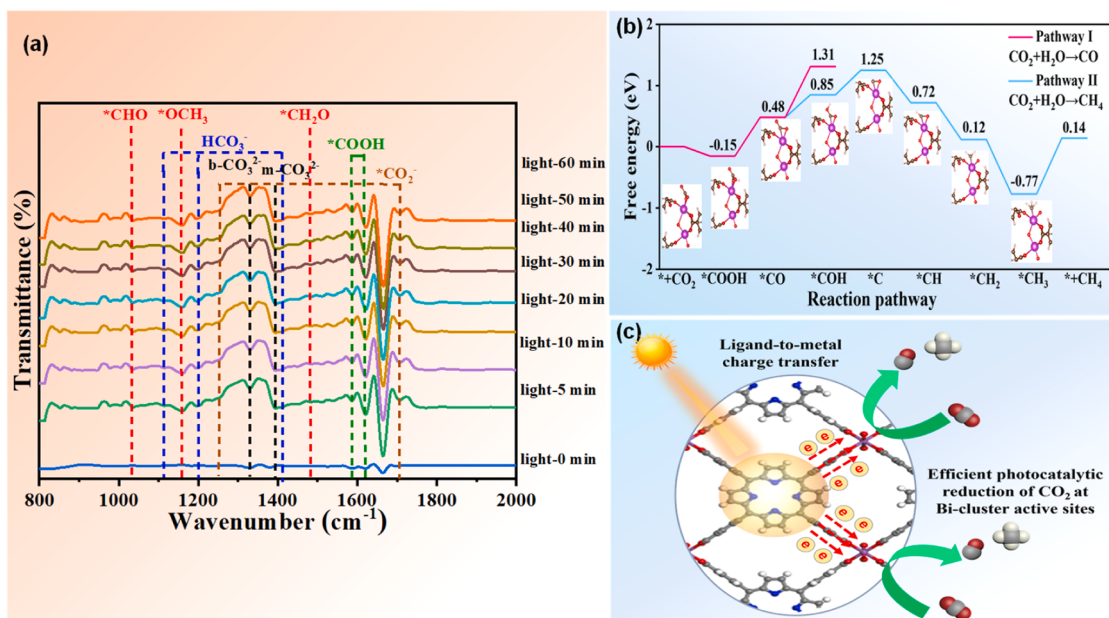


Fig. 6. (a) In-situ FT-IR spectra of SC-Bi-PMOF-6 h under light irradiation after purging with CO_2 and H_2O vapor. (b) The Gibbs free energy change (ΔG) and reaction pathways for photocatalytic CO_2 reduction to CO and CH_4 over Bi-PMOFs. (c) The schematic of photocatalytic CO_2 reduction on SC-Bi-PMOFs.

4. Conclusion

In summary, a new strategy based on molecular-level modulation has been utilized in low temperature rapid synthesis of Bi-PMOFs with well-exposed active sites. This novel strategy takes full advantage of chemical and physical synergistic effect of sc CO_2 , wherein the physical high-diffusion and anti-solvent property accelerate the mass transport and promote rapid Bi-PMOFs crystal growth at low temperature, as well as the CO_2 chemical coordination facilitates the synthesis of 2D Bi-PMOF nanosheets. With regards to the composition and structure, SC-Bi-PMOFs combine many advantages of high accessible active sites, fast electron/mass transfer capability, and unique coordination environment around active sites, thus endowing them superior photocatalytic CO_2 reduction activity. This work lights a new beacon for rapid and efficient construction of various MOFs with abundant active sites, opening up opportunities for practical applications in photocatalysis.

CRediT authorship contribution statement

Weiqian Kong: Resources, Formal analysis. **Pengfei Yan:** Data curation. **Xiaoli Zheng:** Writing – review & editing, Supervision, Funding acquisition, Data curation. **Wenzhuo Wu:** Visualization, Software, Resources, Data curation. **Bin An:** Software. **Yunpeng Zhang:** Resources. **Bo Gao:** Data curation. **Zubin Wang:** Visualization. **Mingjie Cheng:** Writing – original draft, Investigation, Data curation. **Qingchao Li:** Formal analysis. **Qun Xu:** Writing – review & editing, Funding acquisition.

Declaration of Competing Interest

The authors declare that they have no known competing financial interests or personal relationships that could have appeared to influence the work reported in this paper.

Data availability

Data will be made available on request.

Acknowledgements

We are grateful to the National Natural Science Foundation of China (No. 21703207, U2004208 and 21773216), and the China Postdoctoral Science Foundation (No. 2018T110738 and 2017M622363), and the Henan Postdoctoral Research Foundation (No. 001702056). State Key Laboratory of Coking Coal Resources Green Exploitation, Zhengzhou University, Zhengzhou 450001, China.

Appendix A. Supporting information

Supplementary data associated with this article can be found in the online version at doi:10.1016/j.apcatb.2024.124097.

References

- [1] G. Cai, P. Yan, L. Zhang, H.-C. Zhou, H.-L. Jiang, Metal–organic framework-based hierarchically porous materials: synthesis and applications, *Chem. Rev.* 121 (2021) 12278–12326.
- [2] M. Rubio-Martinez, C. Avci-Camur, A.W. Thornton, I. Imaz, D. Maspoch, M.R. Hill, New synthetic routes towards MOF production at scale, *Chem. Soc. Rev.* 46 (2017) 3453–3480.
- [3] N. Stock, S. Biswas, Synthesis of metal-organic frameworks (MOFs): routes to various mof topologies, morphologies, and composites, *Chem. Rev.* 112 (2012) 933–969.
- [4] Y. Fu, Y. Yao, A.C. Forse, J. Li, K. Mochizuki, J.R. Long, J.A. Reimer, G. De Paépe, X. Kong, Solvent-derived defects suppress adsorption in MOF-74, *Nat. Commun.* 14 (2023) 2386.
- [5] Y. Gu, Y.-n Wu, L. Li, W. Chen, F. Li, S. Kitagawa, Controllable modular growth of hierarchical MOF-on-MOF architectures, *Angew. Chem. Int. Ed.* 56 (2017) 15658–15662.
- [6] J. Cao, Z.-h Yang, W.-p Xiong, Y.-y Zhou, Y.-r Peng, X. Li, C.-y Zhou, R. Xu, Y.-r Zhang, One-step synthesis of Co-doped UiO-66 nanoparticle with enhanced removal efficiency of tetracycline: simultaneous adsorption and photocatalysis, *Chem. Eng. J.* 353 (2018) 126–137.
- [7] J.-X. Li, G.-G. Chang, G. Tian, C. Pu, K.-X. Huang, S.-C. Ke, C. Janiak, X.-Y. Yang, Near-linear controllable synthesis of mesoporosity in hierarchical UiO-66 by template-free nucleation-competition, *Adv. Funct. Mater.* 31 (2021) 2102868.
- [8] Y.-R. Lee, M.-S. Jang, H.-Y. Cho, H.-J. Kwon, S. Kim, W.-S. Ahn, ZIF-8: a comparison of synthesis methods, *Chem. Eng. J.* 271 (2015) 276–280.
- [9] Z. Hu, Y. Peng, Y. Gao, Y. Qian, S. Ying, D. Yuan, S. Horike, N. Ogiwara, R. Babarao, Y. Wang, N. Yan, D. Zhao, Direct synthesis of hierarchically porous metal–organic frameworks with high stability and strong bronsted acidity: the decisive role of Hafnium in efficient and selective fructose dehydration, *Chem. Mater.* 28 (2016) 2659–2667.
- [10] S. Naghdi, A. Cherevan, A. Giesriegl, R. Guillet-Nicolas, S. Biswas, T. Gupta, J. Wang, T. Haunold, B.C. Bayer, G. Rupprechter, M.C. Toroker, F. Kleitz, D. Eder,

- Selective ligand removal to improve accessibility of active sites in hierarchical MOFs for heterogeneous photocatalysis, *Nat. Commun.* 13 (2022) 282.
- [11] S. Zhao, Y. Wang, J. Dong, C.-T. He, H. Yin, P. An, K. Zhao, X. Zhang, C. Gao, L. Zhang, J. Lv, J. Wang, J. Zhang, A.M. Khattak, N.A. Khan, Z. Wei, J. Zhang, S. Liu, H. Zhao, Z. Tang, Ultrathin metal–organic framework nanosheets for electrocatalytic oxygen evolution, *Nat. Energy* 1 (2016) 16184.
- [12] G. Chakraborty, I.-H. Park, R. Medishetty, J.J. Vittal, Two-dimensional metal–organic framework materials: synthesis, structures, properties and applications, *Chem. Rev.* 121 (2021) 3751–3891.
- [13] H. Chang, Y. Zhou, S. Zhang, X. Zheng, Q. Xu, CO₂-induced 2D Ni-BDC metal–organic frameworks with enhanced photocatalytic CO₂ reduction activity, *Adv. Mater. Interfaces* 8 (2021) 2100205.
- [14] H. Chang, Y. Zhou, X. Zheng, W. Liu, Q. Xu, Single-layer 2D Ni-BDC MOF obtained in supercritical CO₂-assisted aqueous solution, *Chem. Eur. J.* 28 (2022) e202201811.
- [15] Y. Zhou, P. Yan, S. Zhang, Y. Zhang, H. Chang, X. Zheng, J. Jiang, Q. Xu, CO₂ coordination-driven top-down synthesis of a 2D non-layered metal–organic framework, *Fundam. Res.* 2 (2022) 674–681.
- [16] T. Zheng, X. Kang, Z. Liu, Effective enhancement of capacitive performance by the facile exfoliation of bulk metal–organic frameworks into 2D-functionalized nanosheets, *Nanoscale* 13 (2021) 13273–13284.
- [17] Z.W. Jiang, Y.C. Zou, T.T. Zhao, S.J. Zhen, Y.F. Li, C.Z. Huang, Controllable synthesis of porphyrin-based 2d lanthanide metal–organic frameworks with thickness- and metal-node-dependent photocatalytic performance, *Angew. Chem. Int. Ed.* 59 (2020) 3300–3306.
- [18] J. Liang, H. Yu, J. Shi, B. Li, L. Wu, M. Wang, Dislocated bilayer MOF enables high-selectivity photocatalytic reduction of CO₂ to CO, *Adv. Mater.* 35 (2023) e2209814.
- [19] D. Yang, S. Zuo, H. Yang, Y. Zhou, Q. Lu, X. Wang, Tailoring layer number of 2d porphyrin-based mofs towards photocoupled electroreduction of CO₂, *Adv. Mater.* 34 (2022) e2107293.
- [20] F.-L. Li, P. Wang, X. Huang, D.J. Young, H.-F. Wang, P. Braunstein, J.-P. Lang, Large-scale, bottom-up synthesis of binary metal–organic framework nanosheets for efficient water oxidation, *Angew. Chem. Int. Ed.* 58 (2019) 7051–7056.
- [21] C. Tan, H. Zhang, Wet-chemical synthesis and applications of non-layer structured two-dimensional nanomaterials, *Nat. Commun.* 6 (2015) 7873.
- [22] A. Pustovarenko, M.G. Goesten, S. Sachdeva, M. Shan, Z. Amghouz, Y. Belmakhout, A. Dikhitarenko, T. Rodenas, D. Keskin, I.K. Voets, B. M. Weckhuysen, M. Eddaoudi, L.C.P.M. de Smet, E.J.R. Sudhölter, F. Kapteijn, B. Seoane, J. Gascon, Nanosheets of nonlayered aluminum metal–organic frameworks through a surfactant-assisted method, *Adv. Mater.* 30 (2018) 1707234.
- [23] X. Zhang, L. Chang, Z. Yang, Y. Shi, C. Long, J. Han, B. Zhang, X. Qiu, G. Li, Z. Tang, Facile synthesis of ultrathin metal–organic framework nanosheets for Lewis acid catalysis, *Nano Res.* 12 (2019) 437–440.
- [24] L. Peng, J. Zhang, Z. Xue, B. Han, X. Sang, C. Liu, G. Yang, Highly mesoporous metal–organic framework assembled in a switchable solvent, *Nat. Commun.* 5 (2014) 4465.
- [25] Y. Wang, S. Wang, Z. Li, L. Sun, X. Yang, S. Tang, Synthesis of UiO-66 in supercritical CO₂ and Its Application In Dye Adsorption, *Ind. Eng. Chem. Res.* 60 (2021) 771–780.
- [26] P. López-Domínguez, A.M. López-Periago, F.J. Fernández-Porras, J. Fraile, G. Tobias, C. Domingo, Supercritical CO₂ for the synthesis of nanometric ZIF-8 and loading with hyperbranched aminopolymers. Applications in CO₂ capture, *J. CO₂ Util.* 18 (2017) 147–155.
- [27] A.P. Nelson, O.K. Farha, K.L. Mulfort, J.T. Hupp, Supercritical processing as a route to high internal surface areas and permanent microporosity in metal–organic framework materials, *J. Am. Chem. Soc.* 131 (2009) 458–460.
- [28] H.V. Doan, Y. Fang, Y. Yao, Z. Dong, T.J. White, A. Sartbaeva, U. Hintermair, V. P. Ting, Controlled formation of hierarchical metal–organic frameworks using CO₂-expanded solvent systems, *ACS Sustain. Chem. Eng.* 5 (2017) 7887–7893.
- [29] L. Peng, Q. Guo, C. Song, S. Ghosh, H. Xu, L. Wang, D. Hu, L. Shi, L. Zhao, Q. Li, T. Sakurai, H. Yan, S. Seki, Y. Liu, D. Wei, Ultra-fast single-crystal polymerization of large-sized covalent organic frameworks, *Nat. Commun.* 12 (2021) 5077.
- [30] Y. Li, W. Ma, H. Yang, Q. Tian, Q. Xu, B. Han, CO₂-Assisted synthesis of a crystalline/amorphous NiFe-MOF heterostructure for high-efficiency electrocatalytic water oxidation, *Chem. Comm.* 58 (2022) 6833–6836.
- [31] W.L. Queen, M.R. Hudson, E.D. Bloch, J.A. Mason, M.I. Gonzalez, J.S. Lee, D. Gygi, J.D. Howe, K. Lee, T.A. Darwishi, M. James, V.K. Peterson, S.J. Teat, B. Smit, J. B. Neaton, J.R. Long, C.M. Brown, Comprehensive study of carbon dioxide adsorption in the metal–organic frameworks M₂(dobdc) (M = Mg, Mn, Fe, Co, Ni, Cu, Zn), *Chem. Sci.* 5 (2014) 4569–4581.
- [32] F. Zhang, J. Zhang, B. Zhang, L. Zheng, X. Cheng, Q. Wan, B. Han, J. Zhang, CO₂ controls the oriented growth of metal–organic framework with highly accessible active sites, *Nat. Commun.* 11 (2020) 1431.
- [33] F. Li, G.H. Gu, C. Choi, P. Kolla, S. Hong, T.-S. Wu, Y.-L. Soo, J. Masa, S. Mukerjee, Y. Jung, J. Qiu, Z. Sun, Highly stable two-dimensional bismuth metal–organic frameworks for efficient electrochemical reduction of CO₂, *Appl. Catal. B-Environ.* 277 (2020) 119241.
- [34] M. Cheng, P. Yan, X. Zheng, B. Gao, X. Yan, G. Zhang, X. Cui, Q. Xu, Porphyrin-based Bi-MOFs with enriched surface bi active sites for boosting photocatalytic CO₂ reduction, *Chem. Eur. J.* 29 (2023) e202302395.
- [35] G. Kresse, J. Furthmüller, Efficiency of ab-initio total energy calculations for metals and semiconductors using a plane-wave basis set, *Comp. Mater. Sci.* 6 (1996) 15–50.
- [36] G. Kresse, J. Furthmüller, Efficient iterative schemes for ab initio total-energy calculations using a plane-wave basis set, *Phys. Rev. B* 54 (1996) 11169–11186.
- [37] P.E. Blöchl, Projector augmented-wave method, *Phys. Rev. B* 50 (1994) 17953–17979.
- [38] J.P. Perdew, J.A. Chevary, S.H. Vosko, K.A. Jackson, M.R. Pederson, D.J. Singh, C. Fiolhais, Atoms, molecules, solids, and surfaces: applications of the generalized gradient approximation for exchange and correlation, *Phys. Rev. B* 46 (1992) 6671–6687.
- [39] H.J. Monkhorst, J.D. Pack, Special points for Brillouin-zone integrations, *Phys. Rev. B* 13 (1976) 5188–5192.
- [40] A. Markovits, A. Fahmi, C. Minot, A theoretical study of CO₂ adsorption on TiO₂, *J. Mol. Struct.* 371 (1996) 219–235.
- [41] K.I. Hadjiivanov, D.A. Panayotov, M.Y. Mihaylov, E.Z. Ivanova, K.K. Chakarova, S. M. Andonova, N.L. Drenchev, Power of Infrared and Raman Spectroscopies to Characterize Metal–Organic Frameworks and Investigate Their Interaction with Guest Molecules, *Chem. Rev.* 121 (2021) 1286–1424.
- [42] W.-Q. Li, Y.-X. Wang, J.-Q. Chen, N.-N. Hou, Y.-M. Li, X.-C. Liu, R.-R. Ding, G.-N. Zhou, Q. Li, X.-G. Zhou, Y. Mu, Boosting photo-Fenton process enabled by ligand-to-cluster charge transfer excitations in iron-based metal organic framework, *Appl. Catal. B-Environ.* 302 (2022) 120882.
- [43] E.S. Da Silva, N.M.M. Moura, M.G.P.M.S. Neves, A. Coutinho, M. Prieto, C.G. Silva, J.L. Faria, Novel hybrids of graphitic carbon nitride sensitized with free-base meso-tetrakis(carboxyphenyl) porphyrins for efficient visible light photocatalytic hydrogen production, *Appl. Catal. B-Environ.* 221 (2018) 56–69.
- [44] S. Hussain, Z. Deng, A. Khan, P. Li, Z. Li, Z. Fang, X. Wan, X. Peng, Photothermal responsive ultrathin Cu-TCPP nanosheets/sulfonated polystyrene nanocomposite photo-switch proton conducting membranes, *J. Membr. Sci.* 620 (2021) 118888.
- [45] Y. Zhang, F. Ma, M. Ling, H. Zheng, Y. Wu, L. Li, In-situ constructed indirect Z-type heterojunction by plasma Bi and BiO₂-X-Bi₂O₂CO₃ co-modified with BiOCl@Bi-MOF for enhanced photocatalytic efficiency toward antibiotics, *Chem. Eng. J.* 464 (2023) 142762.
- [46] L. Li, X. Kang, M. He, A. Sheveleva, K. Hu, S. Xu, Y. Zhou, J. Chen, S. Sapchenko, G. Whitehead, I.J. Vitorica-Yrezabal, L. Lopez-Ondrozoa, L.S. Natrajan, E.J. L. McInnes, M. Schröder, S. Yang, F. Tuna, Evolution of bismuth-based metal–organic frameworks for efficient electroreduction of CO₂, *J. Mater. Chem. A* 10 (2022) 17801–17807.
- [47] F. Hasanzandian, M. Moradi, S. Aghaebrahimi Samani, B. Kakavandi, S. Rahman Setayesh, M. Noorisepehr, Effective promotion of g-C₃N₄ photocatalytic performance via surface oxygen vacancy and coupling with bismuth-based semiconductors towards antibiotics degradation, *Chemosphere* 287 (2022) 132273.
- [48] G. Huang, Z.-C. Luo, Y.-D. Hu, Y.-A. Guo, Y.-X. Jiang, S.-J. Wei, Preparation and characterization of iron tetra (pentafluorophenyl)-porphyrin (TPPPP Fe) supported on boehmite (BM), *Chem. Eng. J.* 195–196 (2012) 165–172.
- [49] A.B. Andreeva, K.N. Le, L. Chen, M.E. Kellman, C.H. Hendon, C.K. Brozek, Soft Mode Metal-Linker Dynamics in Carboxylate MOFs Evidenced by Variable-Temperature Infrared Spectroscopy, *J. Am. Chem. Soc.* 142 (2020) 19291–19299.
- [50] D.H. Gibson, Carbon dioxide coordination chemistry: metal complexes and surface-bound species. What relationships? *Coord. Chem. Rev.* 185–186 (1999) 335–355.
- [51] J. Wan, H. Wang, Z. Wu, Y.C. Shun, X. Zheng, D.L. Phillips, Resonance Raman spectroscopy and density functional theory calculation study of photodecay dynamics of tetra(4-carboxyphenyl) porphyrin, *Phys. Chem. Chem. Phys.* 13 (2011) 10183–10190.
- [52] T.M. Cotton, S.G. Schultz, R.P. Van Duyne, Surface-enhanced resonance Raman scattering from water-soluble porphyrins adsorbed on a silver electrode, *J. Am. Chem. Soc.* 104 (1982) 6528–6532.
- [53] I. Strauss, A. Mundstock, D. Hinrichs, R. Himstedt, A. Knebel, C. Reinhardt, D. Dorfs, J. Caro, The interaction of guest molecules with Co-MOF-74: a Vis/NIR and Raman approach, *Angew. Chem. Int. Ed.* 57 (2018) 7434–7439.
- [54] M.Y. Choi, J.A. Pollard, M.A. Webb, J.L. McHale, Counterion-dependent excitonic spectra of tetra(p-carboxyphenyl)porphyrin aggregates in acidic aqueous solution, *J. Am. Chem. Soc.* 125 (2003) 810–820.
- [55] Y. Zhao, X. Cai, Y. Zhang, C. Chen, J. Wang, R. Pei, Porphyrin-based metal–organic frameworks: protonation induced Q band absorption, *Nanoscale* 11 (2019) 12250–12258.
- [56] S. Yang, W. Hu, J. Nyakuchena, C. Fiankor, C. Liu, E.D. Kinigstein, J. Zhang, X. Zhang, J. Huang, Unravelling a long-lived ligand-to-metal cluster charge transfer state in Ce-TCPP metal organic frameworks, *Chem. Comm.* 56 (2020) 13971–13974.
- [57] S. Dai, K.P. Ngoc, L. Grimaud, S. Zhang, A. Tissot, C. Serre, Impact of capping agent removal from Au NPs@MOF core-shell nanoparticle heterogeneous catalysts, *J. Mater. Chem. A* 10 (2022) 3201–3205.
- [58] J.-D. Xiao, H.-L. Jiang, Metal–organic frameworks for photocatalysis and photothermal catalysis, *Acc. Chem. Res.* 52 (2019) 356–366.
- [59] X. Li, B. Kang, F. Dong, Z. Zhang, X. Luo, L. Han, J. Huang, Z. Feng, Z. Chen, J. Xu, B. Peng, Z.L. Wang, Enhanced photocatalytic degradation and H₂/H₂O₂ production performance of S-pCN/WO_{2.72} S-scheme heterojunction with appropriate surface oxygen vacancies, *Nano Energy* 81 (2021) 105671.
- [60] R. Niu, Q. Liu, B. Huang, Z. Liu, W. Zhang, Z. Peng, Z. Wang, Y. Yang, Z. Gu, J. Li, Black phosphorus/Bi₁₉Br₃S₂₇ van der Waals heterojunctions ensure the supply of activated hydrogen for effective CO₂ photoreduction, *Appl. Catal. B-Environ.* 317 (2022) 121727.
- [61] K. Yan, D. Wu, T. Wang, C. Chen, S. Liu, Y. Hu, C. Gao, H. Chen, B. Li, Highly selective ethylene production from solar-driven CO₂ reduction on the Bi₂S₃@In₂S catalyst with In–SV–Bi active sites, *ACS Catal.* 13 (2023) 2302–2312.
- [62] B. Su, Y. Kong, S. Wang, Z. Zuo, W. Lin, Y. Fang, Y. Hou, G. Zhang, H. Zhang, X. Wang, Hydroxyl-bonded Ru on metallic tin surface catalyzing CO₂ reduction with H₂O by infrared light, *J. Am. Chem. Soc.* 145 (2023) 27415–27423.

- [63] S. Karmakar, S. Barman, F.A. Rahimi, S. Biswas, S. Nath, T.K. Maji, Developing post-modified Ce-MOF as a photocatalyst: a detail mechanistic insight into CO₂ reduction toward selective C₂ product formation, *Energ. Environ. Sci.* 16 (2023) 2187–2198.
- [64] S. Karmakar, S. Barman, F.A. Rahimi, T.K. Maji, Covalent grafting of molecular photosensitizer and catalyst on MOF-808: effect of pore confinement toward visible light-driven CO₂ reduction in water, *Energ. Environ. Sci.* 14 (2021) 2429–2440.
- [65] Y. Ma, X. Yi, S. Wang, T. Li, B. Tan, C. Chen, T. Majima, E.R. Wacławik, H. Zhu, J. Wang, Selective photocatalytic CO₂ reduction in aerobic environment by microporous Pd-porphyrin-based polymers coated hollow TiO₂, *Nat. Commun.* 13 (2022) 1400.
- [66] K. Zhu, Q. Zhu, M. Jiang, Y. Zhang, Z. Shao, Z. Geng, X. Wang, H. Zeng, X. Wu, W. Zhang, K. Huang, S. Feng, Modulating Ti t_{2g} orbital occupancy in a Cu/TiO₂ composite for selective photocatalytic CO₂ reduction to CO, *Angew. Chem. Int. Ed.* 61 (2022) e202207600.
- [67] J.-D. Yi, R. Xie, Z.-L. Xie, G.-L. Chai, T.-F. Liu, R.-P. Chen, Y.-B. Huang, R. Cao, Highly Selective CO₂ Electrocatalysis to CH₄ by In Situ Generated Cu₂O Single-type Sites on A Conductive MOF: STabilizing Key Intermediates with Hydrogen Bonding, *Angew. Chem. Int. Ed.* 59 (2020) 23641–23648.
- [68] Z.-B. Fang, T.-T. Liu, J. Liu, S. Jin, X.-P. Wu, X.-Q. Gong, K. Wang, Q. Yin, T.-F. Liu, R. Cao, H.-C. Zhou, Boosting interfacial charge-transfer kinetics for efficient overall CO₂ photoreduction via rational design of coordination spheres on metal-organic frameworks, *J. Am. Chem. Soc.* 142 (2020) 12515–12523.